

# Characterizing Coherent Structures in Bose-Einstein Condensates through Dynamic-Mode Decomposition

Christopher W. Curtis  
Ricardo Carretero  
Matteo Polimeno

## Introduction

With the recent experimental observation of turbulent cascades in a Bose-Einstein Condensate (BEC) [1], it is important to continue to better understand and characterize in as quantitative a means as possible the complex dynamics associated with turbulence in dispersive, nonlinear-wave systems. While small-amplitude states whose statistics remain nearly Gaussian permit a relatively complete analytic characterization of turbulent cascades, embodied in the weak-wave turbulence (WWT) theory initiated in [2] and collected in [3], as noted in [4, 5], the assumptions which one makes to derive results in WWT necessarily must generically break down over long-enough timescales.

This breakdown is best characterized by the formation of long-wavelength, larger-amplitude coherent structures (CSs). In classic, one-dimensional systems, characterizing such structures in terms of solitons is relatively straightforward; see [5]. However, in two-dimensions, and for systems like the defocusing nonlinear Schrödinger equation (NLSE), describing coherent structures in quantitative terms is far more challenging. In the context of BECs, a variety of heuristic metrics to characterize CSs appeared in [6]. In the broader context of WWT, along with classic approaches built around studying qualitative features in Fourier transforms, methods based on tracking spikes in Gaussian curvature of the solution have appeared in [7].

However, as noted in [6], CSs are difficult to visualize in terms of physically measurable variables in BECs. This is due in part to the role that vortices play in BECs, whereby the formation of CSs corresponds to the elimination of vortices. This in some sense removes the most readily identifiable features of the flow, making characterization of the transition away from the WWT state difficult. In this paper, instead, we study the use of Dynamic-Mode Decompositions (DMDs), [8, 9, 10], which is a modal decomposition generated by discrete snap-shots of the temporal evolution of

the BEC. The advantage of DMDs is in their great flexibility due to their essentially being a model-free means of analyzing flows.

As we show, by selecting the most temporally dominant modes from the DMD, we are readily able to characterize coherent states that otherwise remain undetectable in the BEC flow.

## Modelling and Weak-Wave Turbulence

In non-dimensional coordinates (see the Appendix for details on the non-dimensionalization), we model the BEC through the use of a stochastically forced Gross–Pitaevskii (GP), or NLS, equation

$$i\psi_t = -\Delta\psi + |\psi|^2\psi + \gamma_f(\mathbf{x}, t) - i(\nu_h\Delta^{2n} + \nu_l\tilde{\Delta}^{-2n})\psi, \quad \psi(\mathbf{x}, 0) = 0.$$

Note, we always remain in the defocusing, or ‘dark’, case. We solve this equation with periodic boundary conditions, where the common period  $2L \gg 1$  so that we have the equivalent Fourier representation of  $\psi$ ,

$$\psi(\mathbf{x}, t) = \sum_{\mathbf{k}_{mn}} a(\mathbf{k}_{mn}, t) e^{\pi i \mathbf{k}_{mn} \cdot \mathbf{x} / L}.$$

The forcing  $\gamma_f$  is chosen so as to be a spectrally-band limited function

$$\gamma_f(\mathbf{x}, t) = \gamma_0 e^{2\pi i \varphi(t)} \sum_{k_l \leq |\mathbf{k}_{mn}| \leq k_h} e^{\pi i \mathbf{k}_{mn} \cdot \mathbf{x} / L}, \quad \mathbf{k}_{mn} = (m, n),$$

and the phase  $\varphi(t)$  is such that  $\varphi(t) \sim U(0, 1)$  where  $U(0, 1)$  denotes random variables uniformly distributed between 0 and 1. Thus, our forcing is characterized by an injection range of wavenumbers via the choices of  $k_l$  and  $k_h$ . We likewise see that the forcing is unbiased in any particular spatial direction, so that by starting with zero-initial conditions, we see that the solution  $\psi(\mathbf{x}, t)$  will largely mimick the forcing until it has reached a large enough amplitude that nonlinearity, through four-wave mixing, is able to transfer energy across Fourier modes. This is ultimately balanced against the strength of the hyperviscosity characterized by the magnitude of  $\nu_h$  and the hypoviscosity characterized by the magnitude of  $\nu_l$ .

We note that the question of what a ‘large’ domain is is somewhat ambiguous in this problem due to the forcing. Traditionally when modelling a BEC, a length scale is set via the ‘healing-length’ [11], which ultimately determines the width of vortices in the GPE. However, to do this one must have a fixed particle number  $N = \int |\psi|^2 d\mathbf{x}$ , but due to the forcing we necessarily have that

$$\begin{aligned} \frac{1}{2} \frac{dN}{dt} &= \text{Im} \left\{ \int \gamma_f(\mathbf{x}, t) \psi^* d\mathbf{x} \right\} \\ &\quad - \int \psi^* \left( \nu_h \Delta^{2n} + \nu_l \tilde{\Delta}^{-2n} \right) \psi d\mathbf{x} \end{aligned}$$

so that the particle number, and thus length scale, can change with time. Ultimately though, a quasi-equilibrium is achieved through the balance of injection due to the forcing  $\gamma_f$  and the particle removal/energy dissipation due to the hyper/hypoviscosity.

By forcing the system starting from a zero-amplitude state, we hope to ultimately generate a weak-wave turbulence (WWT) state. This is characterized as a nontrivial energy flux in wavenumber. The associated isotropic energy density  $E_d(k, t)$  is given by

$$E_d(k, t) = 2\pi k \omega(k) n(k, t),$$

where  $\omega(k)$  is the dispersion relationship of the GPE, and  $n(k)$  is given by

$$n(k, t) = \left\langle |a(\mathbf{k}_{nm}, t)|^2 \right\rangle, \quad |\mathbf{k}_{nm}| = k.$$

The brackets denote averaging, which in our case, assuming ergodicity, will correspond to temporally averaging the power spectra of the solution of the GPE.

Associated with the energy density is an affiliated energy flux  $\epsilon$  so that

$$\partial_t E_d + \partial_k \epsilon \sim 0.$$

It is one of the major achievements in the WWT theory that one can derive Boltzmann-like kinetic equations describing the evolution of  $n(k, t)$  [3]. Thus, if we characterize the WWT state as one at which the energy density is in quasi-equilibrium so that  $\partial_t E_d \sim 0$ , which therefore implies that  $\partial_t n(k, t) \sim 0$ , we can then distinguish equilibrium profiles of  $n(k, t)$  by whether  $\epsilon \sim 0$  or  $\epsilon \sim c$ , where  $c$  is some constant. The zero case corresponds to no energy flux, thereby describing a thermodynamically steady state associated with the equipartition of energy. It is the non-zero energy flux states which distinguish WWT states, and those that we are most interested in studying.

## Dynamic-Mode Decomposition

We briefly review the details of the DMD for completeness and to better explain later results. In DMD, we assume that any time series of a dynamical quantity of interest, denoted by  $\{\phi_n\}_{n=1}^\infty$ , where  $\phi_n \in \mathbb{R}^M$ , can be described through a linear process mediated via an operator, say  $A$  so that

$$\phi_{n+1} = A\phi_n.$$

We treat  $A$  as essentially unknowable in any direct sense, but by using the affiliated matrices  $V_1^N$ , where

$$V_1^N = \{\phi_1 \cdots \phi_N\}$$

and  $V_2^N = AV_1^N$ , and using a Singular Value Decomposition (SVD) on  $V_1^N$  so that  $V_1^N = U\Sigma W^\dagger$ , we see that

$$U^\dagger AU = \tilde{S}, \quad \tilde{S} = U^\dagger V_2^N W \Sigma^{-1}.$$

Thus by computing the associated eigenvalues and eigenvectors of  $\tilde{S}$ , say  $\mu_j$  and  $\tilde{\phi}_j$  respectively, then for  $N$  large enough with sufficiently controlled spacing in the time-series, these eigenvalues and eigenvectors will approximate those of  $A$ . Likewise, this allows us to write each vector in our time-series as

$$\phi_n = \sum_{j=1}^N b_j \mu_j^n \tilde{\phi}_j + \mathbf{r}_n, \quad \tilde{\phi}_j = U \tilde{\phi}_j,$$

where  $\mathbf{r}_n$  denotes the residual at the  $n^{th}$  sampling time.

## Characterizing Coherent States

### Methodology for Implementing and Analysing the DMD

In order to realize the WWT regimes of the NLS equation, following [6], we run each simulation over a domain of size  $L = 128$  with a total of  $K_T = 256$  modes in each spatial direction. Using a two stage Runge-Kutta scheme with a time step of  $\delta t = .1$ , by simulating up to  $t_f = 1.5 \times 10^4$ , we are able to see the necessary turbulent or mixed dynamics that we are interested in.

With regards to the DMD, we take as the “observable” quantity the magnitude  $|\psi(x, y, t)|$ . Throughout each simulation, we sample every five numerical timesteps, so that the sampling rate is  $\delta t_s = .5$ . We begin sampling at  $t_i = 1.47 \times 10^4$ , so that we sample the last 300 units of time, thereby ensuring we are in fact performing DMD on a fully turbulent or mixed flow. This likewise gives us the approximation

$$|\psi(x, y, t_n^{(s)})| \approx A(t_n^{(s)}) = \sum_{j=1}^N b_j e^{\lambda_j(t_n^{(s)} - t_i)} \tilde{\phi}_j,$$

where

$$\lambda_j = \frac{\log \mu_j}{\delta t_s}, \quad t_n^{(s)} = t_i + n\delta t_s, \quad n \geq 0.$$

Note, the approximation above holds at the discretized points of the spatial mesh used in the numerical simulation of the NLS equation. Thus, if we sample over the entire physical domain, this corresponds then to case where the dimensionality of the DMD vectors  $M = 256^2 \gg 300/.5 = 600$ , so that  $M$  is far larger than the number of time samples taken. As we see in each simulation, typically each DMD generated mode has a corresponding temporal eigenvalue  $\lambda_j$  such that  $\text{Re}(\lambda_j) \leq 2.5 \times 10^{-3}$ , so that every mode is either stationary or transitory.

To perform mode selection, we implement the following strategy. At each discrete sampling time  $t_n^{(s)}$ , we sort the sequence

$$\left\{ \left| b_j e^{\lambda_j(t_n^{(s)} - t_i)} \right| \right\}_{j=1}^N$$

according to magnitude from greatest to least, inducing a mapping between indices, say  $j = f(l; n)$ . Note, by emphasizing the sampling step  $n$ , we are drawing attention to the fact that the sorting map between indices can change at every discrete sampling step. We then select from this sorted listed the minimal number of modes, say  $N_r(n) \leq N$ , such that

$$\frac{\left\| A_{N_r(n)} \left( t_n^{(s)} \right) - \left| \psi(\cdot, \cdot, t_n^{(s)}) \right| \right\|_2}{\left\| \psi(\cdot, \cdot, t_n^{(s)}) \right\|_2} \leq .1,$$

where

$$A_{N_r(n)} \left( t_n^{(s)} \right) = \sum_{l=1}^{N_r(n)} b_{f(l;n)} e^{\lambda_{f(l;n)}(t_n^{(s)} - t_i)} \bar{\phi}_{f(l;n)}$$

Thus  $N_r(n)$  represents the minimal number of maximally sorted modes which represent 90% of the total energy of the NLS equation at  $t_n^{(s)}$ . We likewise define the time dependent compression ratio  $C_r(n) = N_r(n)/N$ . We note that throughout each simulation presented in the remainder of the paper, if we use all of the available modes, the relative error measured above is at most on the order of  $10^{-11}$  over the course of the DMD sampling process, or the norms of the residuals  $\mathbf{r}_n$  are only at worst  $10^{-11} \left\| \psi(\cdot, \cdot, t_n^{(s)}) \right\|_2$ . Thus, taken in its entirety, the DMD provides an extremely accurate reconstruction of the flow over the time which it is applied.

While in some sense an arbitrary choice, we have found the 90% threshold to provide an efficient way to determine the most relevant modes while still providing significant reductions in the compression ratio, thus reflecting the way in which the DMD method is able to capture many of the features of complex flows via relatively low-dimensional representations. Moreover, though the modes of interest can change from sampling step to sampling step, as we see from our results, in practice it is clear that some modes ultimately become consistently more dominant over longer time scales. However, our mode selection scheme also allows us to better understand the dominant processes happening over the length of time of the DMD sampling, thereby allowing for observations of transitory and multiple scales behavior.

Focusing then on those modes which will ultimately dominate towards the end of the DMD process, given that the total time scale over which we perform the DMD is 300 units of non-dimensional time, we define those modes such that  $-.02 \leq \text{Re}(\lambda_j) \leq 2.5 \times 10^{-3}$  to be weakly-transitory. This

choice reflects results from the simulations where it is typical to see the magnitude of the coefficients  $b_j$  to be on the order of  $10^2$  for  $\text{Re}(\lambda_j) \sim -0.02$  and  $10^{-2}$  for  $\text{Re}(\lambda_j) \sim .0025$ . Our definition of a weakly-transitory mode ensures then that an initial amplitude of  $10^2$  is scaled to  $2.5 \times 10^{-1}$ , or just a little over ten percent by the end of the DMD sampling process. Likewise, an initial amplitude of  $10^{-2}$  becomes at most  $.02$ . Thus, by focusing on these weakly-transitory modes, we can focus on those modes which characterize our 90% criterion over longer time scales.

## Modal Descriptions

We first examine the results of the DMD by way of examining the most significant modes which represent the amplitude of the flow at the final time  $t_f = 1.5 \times 10^4$ .

### Weak Wave Turbulence Case

In this case, we take  $k_l = 4$ ,  $k_h = 6$ , and  $\gamma_0 = 2.1 \times 10^{-3}$ . To recreate the WWT results of [6], we keep both hypo and hyperviscosity in place. The results of this are seen in Figures 1. In particular, we see the fully evolved amplitude of the NLS equation at  $t_f$ , i.e.  $|\psi(x, y, t_f)|$ , in Figure 1 (a) compared against the weighted mean of the flow computed via the DMD shown in Figures 1 (b). As seen, we can characterize the WWT regime in part by noting the lack of clear structure in the mean mode. The finer details seen in Figure 1 (a) can in part be recovered by looking beyond the mean mode to higher oscillatory/weakly-transitory modes, seen in Figures 1 (c)-(f). Note, by a plot of a weighted DMD mode, we mean that we plot  $|b_j U \tilde{\phi}_j|$ , thereby allowing us to visualize the spatial structure associated with the mode as well as its relative contribution controlled by the magnitude of  $b_j$  since each mode  $U \tilde{\phi}_j$  is scaled to have unit vector norm.

### Low-Frequency Saturation Case

Through the remaining simulations, we remove the hypoviscosity, and let  $\gamma_0 = 1.6 \times 10^{-3}$ , thereby allowing for saturation in longer-wavelengths to occur. If we continue to look at the relatively low frequency forcing explored above, we expect to see long-wavelength coherent structures to form. It is at this point that we can plainly see the advantage of using the DMD by comparing the fully evolved solution to the NLS equation in Figure 2 (a) to the mean DMD mode in Figure 2 (b). The mean mode clearly identifies a finite number of vortices interacting through a finite amplitude background.

Of interest though is the relative similarity in the finer, higher-frequency features seen in Figures 2 (c)-(f) to those in Figures 1 (c)-(f). As seen, they

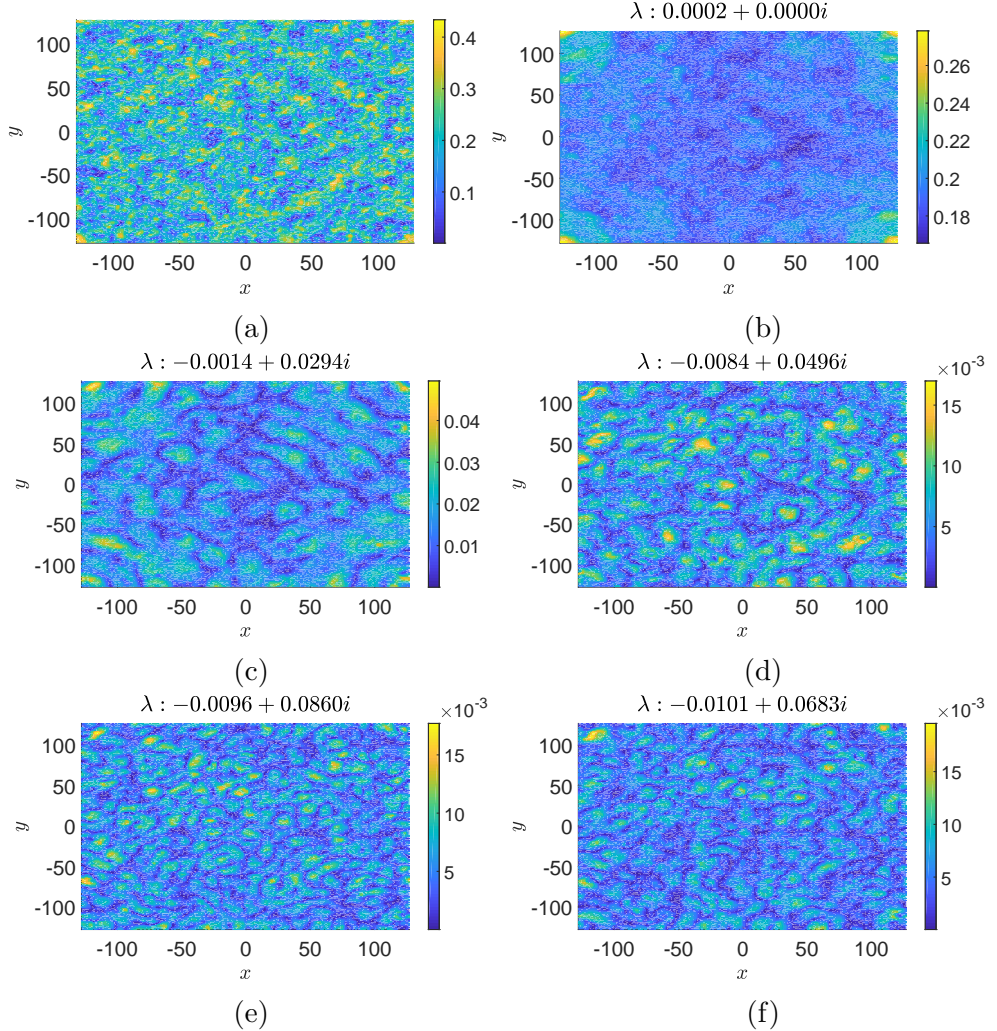


Figure 1: The amplitude  $|\psi(x, y, t_f)|$  (a), weighted mean (b), and next four most significant weakly-transient modes (c)-(f) for  $k_l = 4$ ,  $k_h = 6$ ,  $\gamma_0 = 2.1 \times 10^{-3}$ .

are relatively similar in terms of their overall characteristics, and thus we can characterize the low-frequency saturation case as a long-wave condensed mean with a weakly-turbulent background fluctuating about this mean.

### High-Frequency Saturation Case

We now look at higher-frequency forcing where we let  $k_l = 60$  and  $k_h = 63$ . As in the low-frequency, long-wavelength saturated case above, we see that the mean DMD mode seen in Figure 3 (b) clearly isolates the condensed dynamics obscured through the higher-frequency spatial features in the solu-

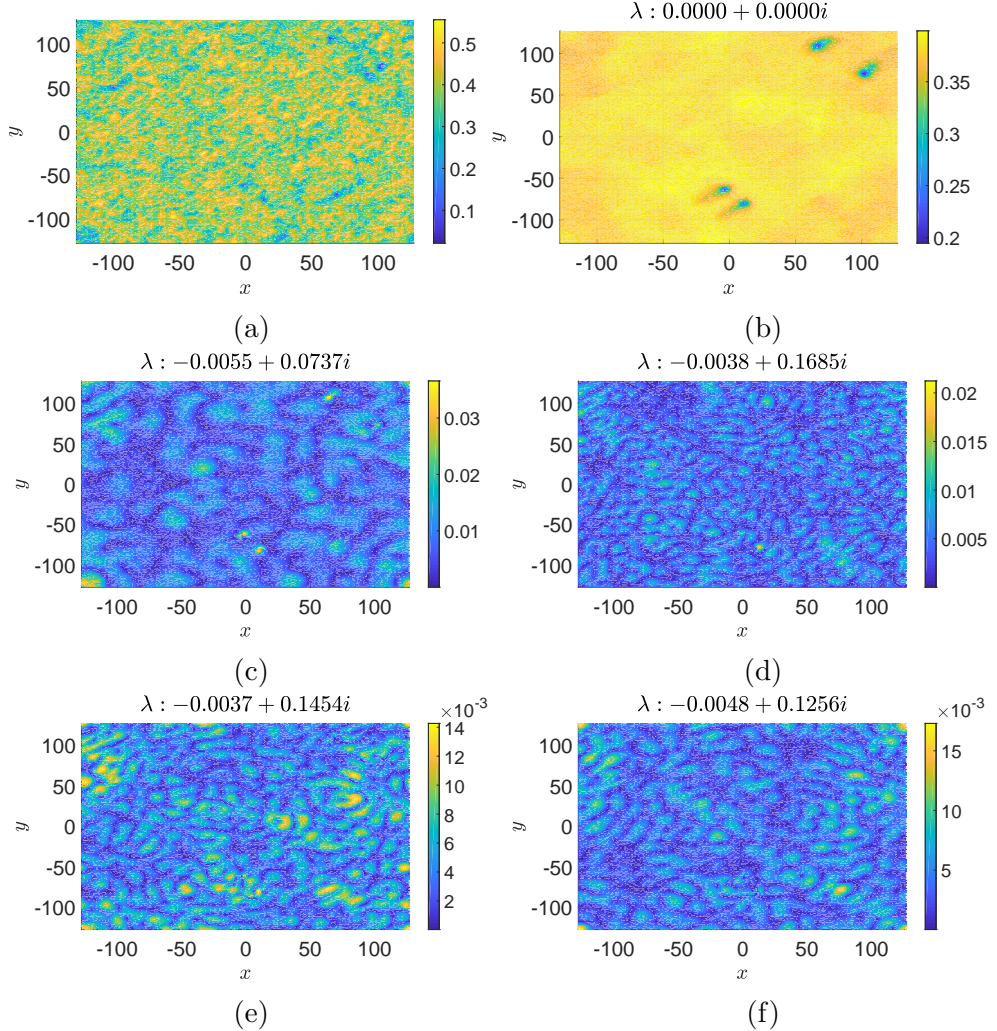


Figure 2: The amplitude  $|\psi(x, y, t_f)|$  (a), weighted mean (b), and next four most significant weakly-transient modes (c)-(f) for  $k_l = 4$ ,  $k_h = 6$ ,  $\gamma_0 = 1.6 \times 10^{-3}$ .

tion to the NLS equation seen in Figure 3 (a). In contrast the low-frequency forcing case above though, we see in the higher-order modes in Figures 3 (c)-(f), far sharper, or higher-frequency, spatial features, thus clearly reflecting the different forcing mechanism in play in this simulation.

### Comparison Across Flows via Spectral Characteristics

We now compare the spectral characteristics and compression ratios of the weak-wave turbulence (WWT), low-frequency saturation (LFS), and high-frequency saturation (HFS) cases studied above. Here, we focus less on iso-

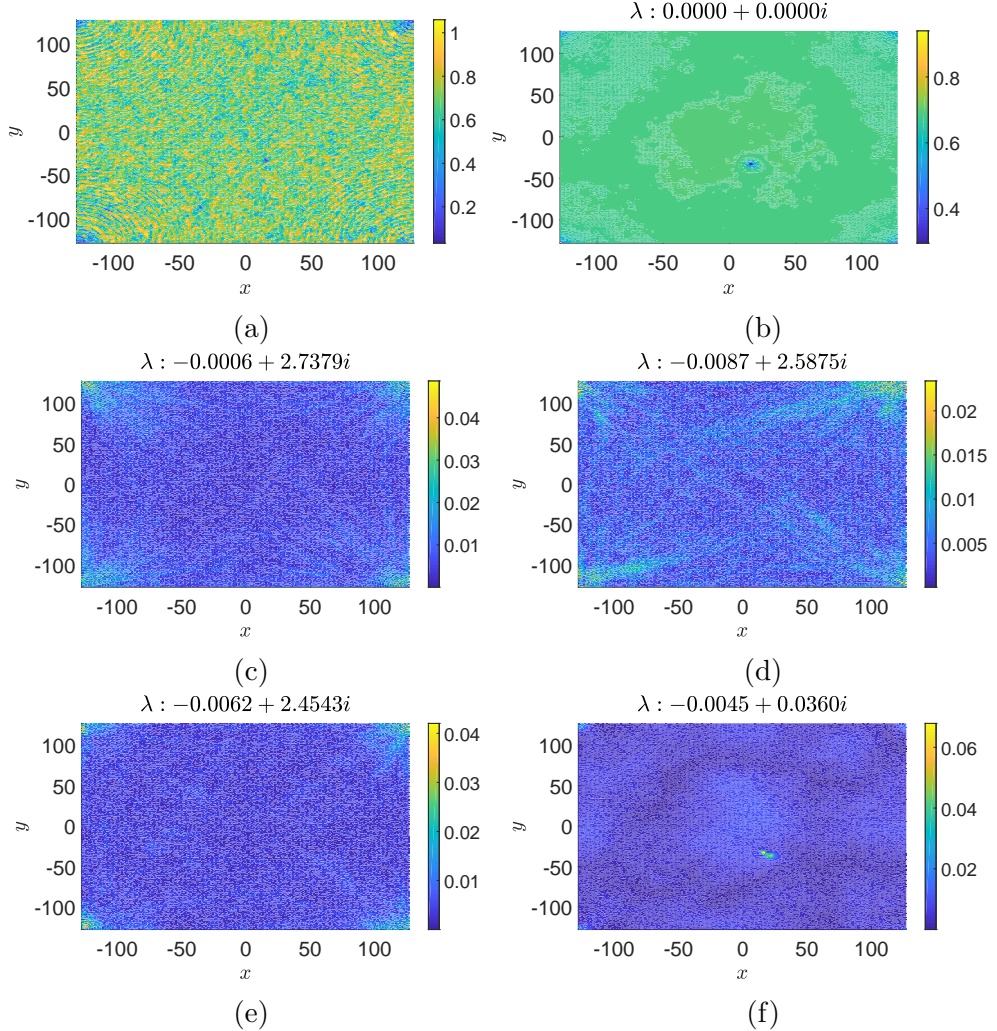


Figure 3: The amplitude  $|\psi(x, y, t_f)|$  (a), weighted mean (b), and next four most significant weakly-transient modes (c)-(f) for  $k_l = 60$ ,  $k_h = 63$ ,  $\gamma_0 = 1.6 \times 10^{-3}$ .

lating some relatively small number of modes and more examine the characteristic responses of each measured quantity across the different flows thereby allowing for the identification of classifying features that may not be as readily apparent given the overall complexity of each flow. As seen in Figures 4 (a), (c), and (e) among those modes which are weakly-transitory, the mean always begins as the dominant mode with respect to its magnitude of  $|b_j|$ . Likewise, we see from Figures 4 (b), (d), and (f) that the higher temporal frequencies of oscillation correspond to smaller magnitudes of  $|b_j|$ , reflecting a kind of energy decay in time akin to what one usually sees via Fourier transforms in time or space. However, focusing on the

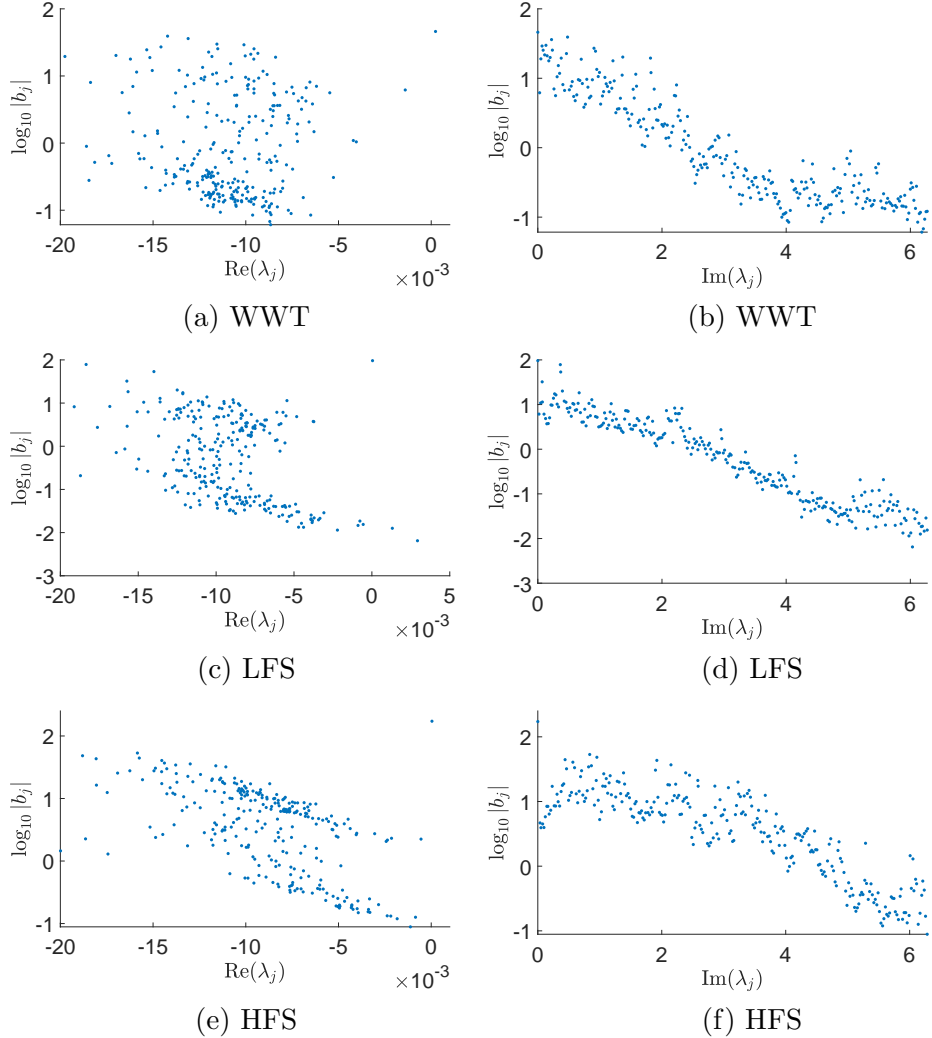


Figure 4: Plot of the real part of  $\lambda_j$  against  $\log_{10} |b_j|$  for the WWT (a), low-frequency saturated (c), and high-frequency saturated (e) regimes and the plot of the imaginary part of  $\lambda_j$  against  $\log_{10} |b_j|$  for the WWT (b), low-frequency saturated (d), and high-frequency saturated (f) regimes.

regime of weakly-transitory modes, we see marked differences in the spread of the magnitudes of  $|b_j|$  with respect to the real part of the eigenvalues  $\lambda_j$ . Thus, the way in which weakly transitory effects manifest themselves are distinguished in the different classes of flows.

The impact of this manifests itself in the different dynamics and long time behavior of the compression ratio  $C_r(n)$  seen in Figures 5 (b), (d), and (f). As seen, the greater complexity of the WWT flow necessitates larger, and at times, more erratic numbers of modes in order to maintain

the 90 % threshold used for modal selection. However, we also see the greater complexity of the HFS case in comparison to the LFS case by way of the overall larger compression ratio needed in the HFS case. A partial explanation for this is that in the HFS case in order for energy to transfer to the longer wavelengths one must first form the higher frequency, spindle like structures seen in Figures 3 (c)-(f). Lastly, we note the presence of jumps in the compression ratio which clearly correspond to the more transitory modes, determined from examining the most leftward eigenvalues in Figures 5 (a), (c), and (e).

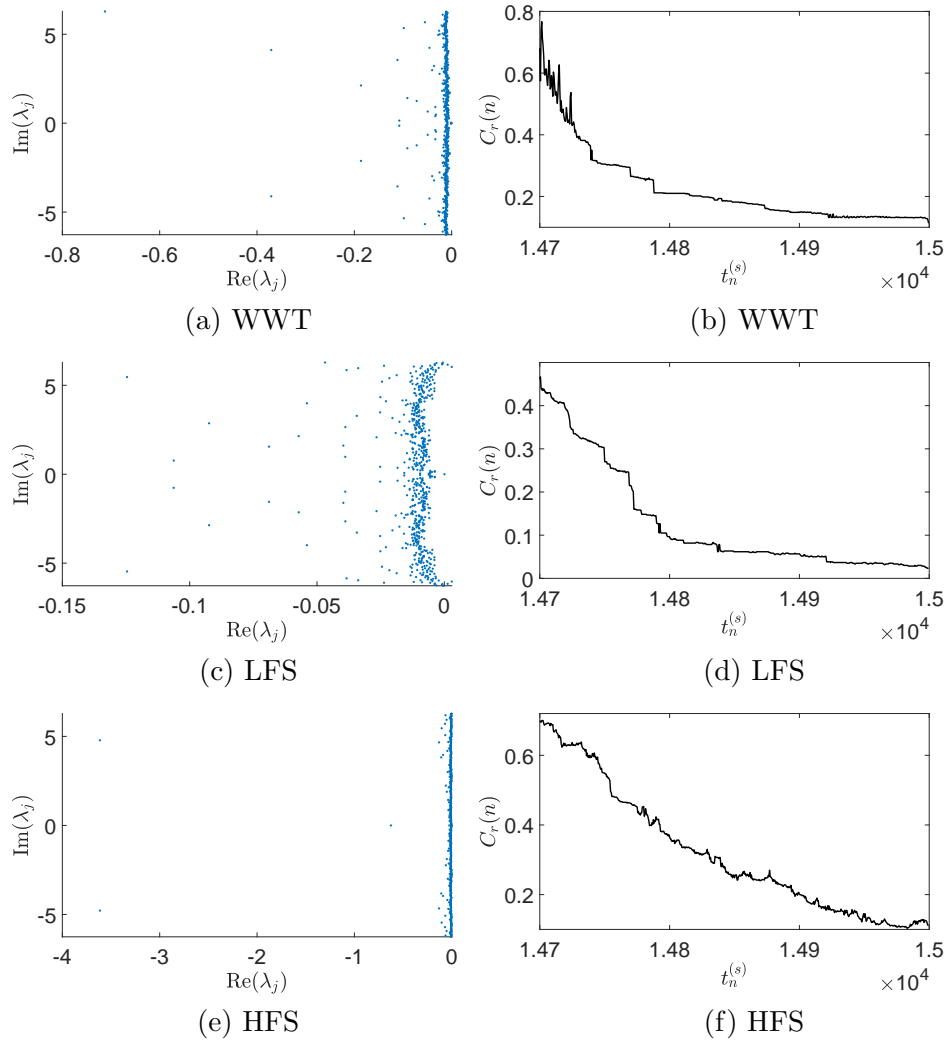


Figure 5: Plot of the full spectrum for the WWT (a), low-frequency saturated (c), and high-frequency saturated (e) regimes and the compression ratio  $C_r(n)$  for the WWT (b), low-frequency saturated (d), and high-frequency saturated (f) regimes.

## Conclusion

## Appendix

With units, our model of a BEC is given by the following Gross–Pitaevskii equation (GPE)

$$i\hbar\psi_t = -\frac{\hbar^2}{2m}\Delta\psi + g|\psi|^2\psi, \quad g = \frac{4\pi\hbar^2 a_s}{m}$$

where  $a_s$  is the ‘scattering length’, and with the clear understanding that  $|\psi|^2 dx dy$  describes probabilities in the sense that

$$\int |\psi|^2 dx dy = N,$$

where we take  $N$  to be the total number of particles under consideration. Introducing the non-dimensionalizations

$$\tilde{x} = x/\lambda, \quad \tilde{y} = y/\lambda, \quad \tilde{t} = t/T,$$

and choosing

$$\lambda^2 = \frac{1}{8\pi|a_s|}, \quad T = \frac{m}{4\pi\hbar|a_s|},$$

then gives us

$$i\psi_t = -\Delta\psi + \sigma|\psi|^2\psi, \quad \sigma = \text{sgn}(a_s).$$

## References

- [1] N. Navon, A.L. Gaunt, R.P. Smith, and Z. Hadzibabic. Emergence of a turbulence cascade in a quantum gas. *Nature*, 539:72–75, 2016.
- [2] V.E. Zakharov. Weak turbulence in media with decay dispersion law. *Zh. Prikl. Mekh I Tekhn. Fiz.*, 4:35, 1965.
- [3] S. Nazarenko. *Wave Turbulence*. Springer, New York, NY, 2011.
- [4] A.C. Newell, S. Nazarenko, and L. Biven. Wave turbulence and intermittency. *Physica D*, 152:520–550, 2001.
- [5] D. Cai, A.J. Majda, D.W. McLaughlin, and E.G. Tabak. Dispersive wave turbulence in one dimension. *Physica D*, 152:551–572, 2001.
- [6] S. Nazarenko and M. Onorato. Wave turbulence and vortices in Bose–Einstein condensation. *Physica D*, 219:1–12, 2006.
- [7] N. Mordant and B. Miquel. Intermittency and emergence of coherent structures in wave turbulence of a vibrating plate. *Phys. Rev. E*, 96:042204, 2017.

- [8] P. Schmid. Dynamic mode decomposition of numerical and experimental data. *J. Fluid Mech.*, 656:5–28, 2010.
- [9] M.O. Williams, I. G. Kevrekidis, and C. W. Rowley. A data-driven approximation of the Koopman operator: extending dynamic mode decomposition. *J. Nonlin. Sci.*, 25:1307–1346, 2015.
- [10] J.N. Kutz, S.L. Brunton, B.W. Brunton, and J.L. Proctor. *Dynamic Mode Decomposition: Data-driven modeling of complex systems*. SIAM, Philadelphia, PA, 2016.
- [11] C.J. Pethick and H. Smith. *Bose-Einstein Condensation in Dilute Gases*. Cambridge University Press, Cambridge, 2011.